A Study of Sea Ice Topography in the Weddell and Ross Seas Using Dual Polarimetric TanDEM-X Imagery

Lanqing Huang[1] and Irena Hajnsek[1,2]

[1]Institute of Environmental Engineering, Swiss Federal Institute of Technology in Zürich (ETH), Zürich, 8093, Switzerland
[2]Microwaves and Radar Institute, German Aerospace Center (DLR), Wessling, 82234, Germany

Correspondence: Lanqing Huang (huang@ifu.baug.ethz.ch)

Abstract. The sea ice topography is essential for understanding the interactions within the air-ocean-ice system. Single-pass interferometric synthetic aperture radar (InSAR) allows for the generation of digital elevation model (DEM) over the drift sea ice. However, accurate sea ice DEMs (i.e., snow freeboard) derived from InSAR are impeded due to the radar signals penetrating the snow and ice layers. This research introduces a novel methodology for retrieving sea ice DEMs using dual-polarization interferometric SAR images, considering the variation in radar penetration bias across multiple ice types. The accuracy of the method is verified through photogrammetric measurements, demonstrating the derived DEM with a root-mean-square error of $0.26\,\mathrm{m}$ over a $200 \times 19\,\mathrm{km}$ area. The method is further applied to broader regions in the Weddell and the Ross Sea, offering new insights into the regional variations of sea ice topography in the Antarctic. We also characterize the non-Gaussian statistical behavior of sea ice elevations using log-normal and exponential-normal distributions. The results suggest that the exponential-normal distribution is superior in the thicker sea ice region (average elevation $> 0.5\,\mathrm{m}$), whereas the two distributions exhibit similar performance in the thinner ice region (average elevation $< 0.5\,\mathrm{m}$). These findings offer an in-depth representation of sea ice elevation and roughness in the Weddell and Ross Sea, which can be conducted in time series data to comprehend sea ice dynamics, including its growth and deformation.

1 Introduction

Sea ice topography refers to the ice shape, height, and large-scale roughness at the meter scale. It encompasses a variety of ice features, including rafted ice, ridges, rubble fields, and hummocks, all of which contribute to the intricate nature of sea ice topography (Weeks and Ackley, 1986). The presence of snow cover atop the ice surface further influences the topographic characteristics, adding another layer of complexity to the overall sea ice topography (Massom et al., 2001). Sea ice topography can be described through digital elevation models (DEM). The DEM stands as an essential input into sea ice dynamic modeling, important for determining the air-ice drag coefficient and momentum flux (Garbrecht et al., 2002; Castellani et al., 2014; Nghiem et al., 2022). Moreover, the DEM (i.e., snow freeboard), together with snow depth and the assumed values of snow, ice, and seawater densities, enables the determination of sea ice thickness (Kwok and Kacimi, 2018). This estimation is crucial in assessing the impacts of climate change on sea ice dynamics. Furthermore, mapping sea ice topography is paramount for safe navigation in polar oceans. By providing information on ice deformation and identifying safe routes, accurate sea ice

25 topography maps contribute to ensuring the safety and efficiency of ship navigation in challenging environments (Dammann et al., 2017).

Sea ice elevation has been measured using laser altimeter mounted on different platforms, including helicopters (Dierking, 1995), aircraft such as IceBridge (Petty et al., 2016), and satellites like ICESat-1 (Zwally et al., 2008) and ICESat-2 (Kacimi and Kwok, 2020). These laser altimeters provide high-spatial resolution ($< 1\,\mathrm{m}$) in measuring sea ice elevation. However, limited

30 spatial coverage and long revisit times (e.g., 91 days for ICESat-2) restrict their capacity for consistent and comprehensive sea ice monitoring. In recent decades, synthetic aperture radar (SAR) has been of significant importance for Earth observation, offering a balance between spatial resolution (meters to tens of meters) and swath coverage (tens to hundreds of kilometers). SAR is unaffected by weather conditions or daylight limitations, enabling consistent data acquisition with a revisit time of around ten days. Notably, the advent of single-pass interferometric SAR (InSAR) sensors, exemplified by TanDEM-X, presents

35 an unprecedented opportunity to generate sea ice DEMs for drift (Dierking et al., 2017) and landfast (Yitayew et al., 2018) sea ice.

Nevertheless, the InSAR-derived DEM can be affected by the microwave penetration into the snow and ice layers. Dry snow can have penetration depths up to hundreds of wavelengths (Guneriussen et al., 2001). For X-band SAR, the penetration into younger ice, such as new and first-year ice, is minimal due to the high salinity of the ice surface (Hallikainen and Winebrenner,

40 1992). On the other hand, for older and desalinated ice, such as multi-year ice, the penetration depth varies from $0-1\,\mathrm{m}$ depending on the temperature and salinity (Hallikainen and Winebrenner, 1992; Huang et al., 2021). To account for the scattering mechanism from the volumes (snow and ice) and layers (snow-ice-water interfaces), a two-layer-plus-volume (TLPV) model (Huang et al., 2021) has been developed to determine the penetration depth over snow-covered old ice in the Antarctic. The model improves the precision of sea ice topographic mapping by offsetting the InSAR phase center to the top surface.

45 SAR polarimetry complements interferometry by providing valuable insights into scattering processes and has proven useful for characterizing sea ice properties (Winebrenner et al., 1995; Ressel et al., 2016; Singha et al., 2018). For old and deformed ice, a radar theory has been developed to examine the relationship between scattering mechanisms and sea ice DEM (Nghiem et al., 2022), resulting in a geophysical model function based on co-polarimetric coherence for retrieving sea ice DEM (Huang et al., 2022). These findings emphasize the significance of integrating polarimetric and interferometric information for precise

50 sea ice topography mapping using SAR imagery.

Given the variations in the microwaves' penetration depth into snow and ice, deriving sea ice DEM from SAR imagery over a broad spatial scale encompassing diverse ice types is still constrained. In this study, we develop an innovative two-step method to generate sea ice DEM across multiple ice types using machine learning and polarimetric-interferometry SAR techniques. The initial step involves the development of a random forest classifier using specific SAR features to categorize sea ice into

55 two groups: younger ice (YI) and older ice (OI), based on the penetration depth of microwaves. Subsequently, a sea ice DEM is created for each ice type. In the case of YI, standard InSAR processing is applied to determine the elevation. For OI, a novel inversion algorithm is proposed to estimate the parameters of the developed TLPV model (Huang et al., 2021). This allows for correcting penetration bias in the InSAR signal over OI, resulting in a precise sea ice DEM. We validate the proposed method against the photogrammetric DEM from the IceBridge aircraft. A root-mean-square error (RMSE) of $0.26\,\mathrm{m}$ between

60 the derived DEM and reference data signifies a precise elevation mapping for both YI and OI. Throughout the paper, "sea ice elevation" is the entire vertical height (including snow depth) above the local sea surface.

We further implement the proposed two-step approach to 162 SAR images covering 12 segments (each covering an area of $\sim 500 \times 20\,\mathrm{km}$) in the Weddell and Ross Sea. This allows a broad mapping of sea ice elevation and roughness, offering new insights into the topographic patterns of sea ice at a large spatial scale. Note that the roughness in this study refers to

65 the macroscale roughness, which is defined as the standard deviation of elevation within $50 \times 50\,\mathrm{m}$ window. We analyze the variation in sea ice elevation and roughness along the southwards direction and associate it with the variation in sea ice classes obtained from the Ice Chart. The statistics of sea ice elevations over various regions are modeled using the log-normal and exponential-modified normal distributions. The findings enhance our understanding of sea ice formation and dynamics and can be used to interpret geophysical parameters associated with sea ice topography.

70 The paper is structured as follows. Section 2 describes the data sets and data processing procedures. The two-step approach for sea ice DEM retrieval is introduced in Sect. 3. The retrieval results and interpretation of topographic characteristics are discussed in Sect. 4. Finally, Section 5 concludes the study.

2 Data sets and processing

2.1 Study area

75 The region of interest includes both the Weddell Sea and the Ross Sea, as shown in Fig. 1. The SAR footprints over the two seas are zoomed-in in boxes A and B, respectively. The footprints comprise 12 segments, each corresponding to a sequence of SAR acquisitions at almost the same time stamp. The segments will be referred to as W1-U, W1-L, W2-U, W2-L, W3-U, W3-L, W4, W5-U, W5-L, R1-U, R1-L, and R5 in the following sections for conciseness.

2.2 SAR Imagery

80 The TanDEM-X is a SAR interferometer that operates as a bistatic single-pass system, capable of acquiring two images simultaneously (Krieger et al., 2007). The two images are co-registered single-look complex products, which can be processed to derive sea ice DEM through interferometry.

In the study, we collected 162 SAR images over the twelve segments in StripMap mode in dual-pol channels (HH and VV). The pixel spacing is around $0.9\,\mathrm{m} \times 2.7\,\mathrm{m}$ in slant range and azimuth. The acquisition time and the number of images for each

85 segment are listed in Table 1. The incidence angle (InA) is measured at the center of the scene, and the height of ambiguity (HoA) corresponds to an interferometric phase change of 2π.

The multilooking processing was conducted using a 4×12 window, resulting in a $\sim 10 \times 10\,\mathrm{m}$ pixel spacing in azimuth and range. The backscattering intensity $\sigma_{\mathrm{measure}}$ of the images includes additive thermal noise, which can be described by the noise equivalent sigma zero (NESZ) and assumed to be uncorrelated with the signal (Nghiem et al., 1995). We denoised

90 backscattering intensities for the different polarizations (i.e., HH, VV, Pauli-1 (HH+VV), and Pauli-2 (HH-VV)) by subtracting
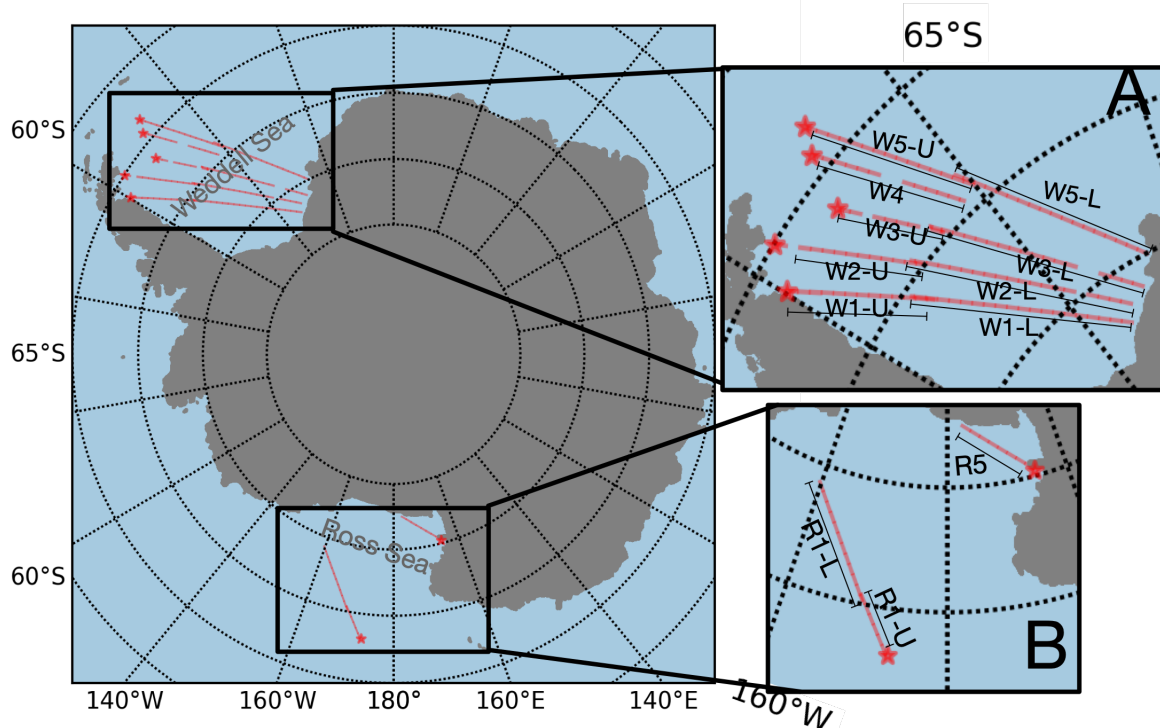
Figure 1. Geolocation of the study area. The northernmost positions in each segment are marked with star symbols and serve as reference points for calculating the relative distance in Sec. 4.2.

the noise equivalent sigma zero (NESZ) from the $\sigma_{\mathrm{measure}}$ (Huang et al., 2022). These denoised intensities are used in the following sections.

2.3 Optical Digital Mapping System (DMS) data

With an objective to investigate Antarctic sea ice topography, Operation IceBridge (OIB) and TanDEM-X Antarctic Science

95 Campaign (OTASC) (Nghiem et al., 2018) was successfully carried out along a portion of the W1, shown in Fig. 2a. Equipped with a digital mapping system (DMS), the OIB aircraft captured optical images (Dominguez, 2010, updated 2018) and generated DEM using photogrammetric techniques at a spatial resolution of approximately $40\,\mathrm{cm} \times 40\,\mathrm{cm}$ (Dotson and Arvesen., 2012, updated 2014). The DMS acquisitions occurred between 17:45 and 18:44 UTC on October 29, 2017. Figure 2b and c showcase DMS optical images over specific areas, highlighting a diverse range of sea ice features, including ridges, deformed

100 ice, smooth ice with snow cover, and snow-free ice.

Table 1. Summary of SAR acquisitions and Ice Charts over the study area.

Segment	Number of SAR images	SAR acquisition time	HoA(m)	InA(∘)	Weekly average Ice Charts (starting date)
W1-L	20	2017-10-24T23:30	$30-35$	29	2017-10-19
W1-U	13	2017-10-29T23:41	$33-35$	35	2017-10-26
W2-L	19	2017-10-25T23:13	$30-35$	29	2017-10-19
W2-U	12	2017-10-30T23:23	$32-34$	35	2017-10-26
W3-L	18	2017-10-26T22:56	$30-35$	29	2017-10-26
W3-U	8	2017-11-22T23:05	$36-37$	35	2017-11-16
W4	12	2017-11-01T22:49	$32-34$	35	2017-10-26
W5-L	18	2017-11-02T22:30	$30-34$	29	2017-11-02
W5-U	15	2017-10-27T22:41	$31-34$	35	2017-10-26
R1-L	12	2017-11-11T07:16	$33-35$	31	2017-11-09
R1-U	6	2017-10-25T07:25	$34-35$	36	2017-10-19
R5	9	2017-11-07T09:58	$40-42$	35	2017-11-02
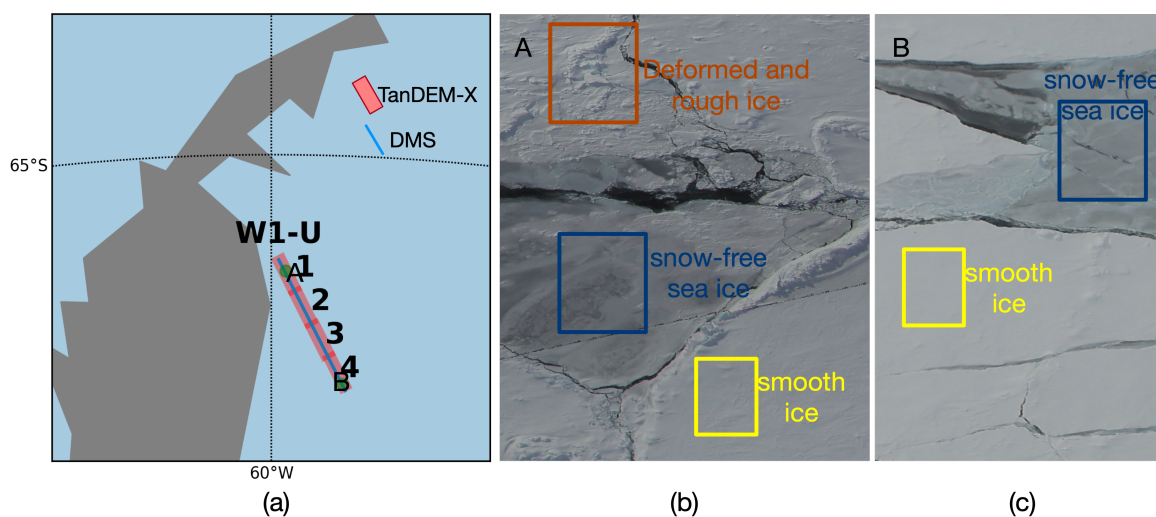
Figure 2. (a) Geolocation of DMS measurements superimposed on four SAR footprints in segment W1-U. Zoomed-in views of DMS digital images at points A and B (green dots) are displayed in (b) and (c), respectively.

Table 2. Stage of develops for ice type categories (U.S. National Ice Center., 2020).

Ice Stage of development	Thickness (cm)	Ice type
New ice	< 10	
Nilas, ice rind	< 10	
Young ice	$10- < 30$	Thin ice (TI)
Gray ice	$10- < 15$	
Gray-white ice	$15- < 30$	
FYI	$\geq 30 - 200$	
Thin FYI	$30- < 70$	
Medium FYI	$70- < 120$	First-year ice (FYI)
Thick FYI	≥ 120	
Old ice		
2nd year ice	N/A	Multiyear ice (MYI)
multiyear ice		

In this study, we geocoded the DMS DEM to match the same coordinates and resolution as the multilooked SAR image, which is approximately $10 \times 10\,\text{m}$ in both range and azimuth. The calibration of the DMS DEM to the local sea level was accomplished through a manual process involving the selection of the water surface from DMS images (Huang et al., 2021).

As the sea ice is constantly moving, co-registration is crucial to compensate for the time lag (~ 6 hours) between the DMS

105 sensor and TanDEM-X. To achieve this, we carefully aligned the two data by identifying distinctive sea ice features in both optical and SAR images (Huang et al., 2021, 2022). The co-registered DMS DEM is used as reference data in this study.

2.4 Ice Charts

Weekly sea ice concentration charts (referred to as Ice Charts hereafter) represent the average stage of development along with respective concentrations over a 7-day period (U.S. National Ice Center., 2020). The Ice Charts covering the date of SAR

110 acquisitions are listed in Table 1.

The Ice Charts are provided in Shapefile format as grids with a spatial resolution of $10 \times 10\,\text{km}$. For each specified latitude and longitude, three ice concentration values are given, each corresponding to a different stage of ice development. Details of these stages and their corresponding thicknesses can be found in the first and second columns of Table 2, respectively. The postprocessing of the Ice Charts consists of two steps. First, we categorized the three stages of ice into thin ice (TI), first-year

115 ice (FYI), and multiyear ice (MYI) types according to the third column of Table 2. Next, we calculated the average ice type by $\sum_{i=1}^{3} IC_i \times IT_i$, where IC_i denotes the ice concentration value and IT_i stands for the ice type index for each stage i. Ice-type indices (IT_i) are assigned as 0 for TI, 1 for FYI, and 2 for MYI.

2.5 SAR interferometry

Single-pass interferometer acquires two simultaneous observations, denoted as s_1 and s_2. The complex interferogram γ and the interferometric phase ϕ_γ can be described as (Cloude, 2010)

$$\gamma = s_1 s_2^* \tag{1}$$

$$\phi_\gamma = \arg\{s_1 s_2^*\} \tag{2}$$

The further processing of ϕ_γ includes flat earth removal, interferogram filtering, low-coherence area mask, and phase unwrapping (Huang and Hajnsek, 2021). The resulting $\phi_\gamma^{'}$ is converted to height by

$$h_{\text{InSAR}} = h_a \frac{\phi_\gamma^{'}}{2\pi} \tag{3}$$

where h_{InSAR} is the height of InSAR phase center and h_a is the HoA related to the InSAR baseline configuration provided in Table 1.

The complex interferometric coherence $\tilde{\gamma}_{\text{InSAR}}$ between the two images can be estimated by (Cloude, 2010)

$$\tilde{\gamma}_{\text{InSAR}} = \gamma_{\text{InSAR}} \cdot e^{i\phi_\gamma} = \frac{<s_1 s_2^*>}{\sqrt{<s_1 s_1^*><s_2 s_2^*>}} \tag{4}$$

where the symbol $< . >$ denotes an ensemble average within a 4×12 multilooking window. Pixels with $\gamma_{\text{InSAR}} < 0.3$ were designated as water areas and excluded from further processing. The above interferometric processing was carried out using the GAMMA software.

2.6 SAR polarimetry

SAR Polarimetry reflects scattering mechanisms and has been proven as a proxy for characterizing sea ice properties (Wakabayashi et al., 2004; Ressel et al., 2016; Huang and Hajnsek, 2021; Singha et al., 2018; Nghiem et al., 2022).

2.6.1 Co-polarization ratio

The co-polarization (coPol) ratio (R_{coPol}) measures the backscattering intensity ratio between the dual-pol channels and can be calculated as follows

$$R_{\text{coPol}} = \frac{\sigma_{\text{HH}}}{\sigma_{\text{VV}}} \tag{5}$$

where σ_{HH} and σ_{VV} are denoised SAR backscattering intensity in dual-pol channels in linear scale. R_{coPol} related to the dielectric constant, has been considered as an indicator for ice thickness (Wakabayashi et al., 2004). Additionally, R_{coPol} has been identified as an important feature for discriminating thicker ice and water and is an effective tool for classifying sea ice in X-band SAR imagery (Ressel et al., 2016).

2.6.2 Pauli-polarization ratio

Similarly, we can obtain the Pauli-polarization ratio (R_{pauli}) by

$$R_{\mathrm{Pauli}} = \frac{\sigma_{\mathrm{P1}}}{\sigma_{\mathrm{P2}}} \tag{6}$$

where σ_{P1} and σ_{P2} are denoised SAR backscattering intensity in Pauli-1 and Pauli-2 polarizations in linear scale, respectively.

2.6.3 Complex coPol coherence

The complex coPol correlation $\tilde{\gamma}_{\mathrm{coPol}}$ is calculated as (Lee and Pottier, 2009)

$$\tilde{\gamma}_{\mathrm{coPol}} = \gamma_{\mathrm{coPol}} \cdot e^{i\phi_{\mathrm{coPol}}} = \frac{< s_{\mathrm{VV}} s_{\mathrm{HH}}^* >}{\sqrt{< s_{\mathrm{VV}} s_{\mathrm{VV}}^* >< s_{\mathrm{HH}} s_{\mathrm{HH}}^* >}} \tag{7}$$

where γ_{coPol} is the coPol coherence magnitude and ϕ_{coPol} is the coPol phase. s_{HH} and s_{VV} are single-look complex images in dual-pol channels, respectively.

γ_{coPol} measures the degree of electromagnetic wave depolarization caused by the surface roughness and the volume scattering. This parameter has been shown to be associated with sea ice elevation (Huang and Hajnsek, 2021) and thickness (Kim et al., 2011). ϕ_{coPol} is sensitive to the anisotropic structure of the medium and deviates from $0°$ when the signal delay becomes polarization dependent (Leinss et al., 2014). ϕ_{coPol} has been utilized in retrieving fresh-snow anisotropy over ground (Leinss et al., 2016) and characterizing the topography of snow layer (Huang and Hajnsek, 2021).

3 Methodology

This section introduces an innovative approach for retrieving sea ice elevation across various ice conditions, shown in Fig. 3. The initial step is categorizing sea ice into OI and YI types based on radar penetration depths. The second step involves generating the sea ice DEM using different methods for the two sea ice categories. The two steps are detailed in Sect. 3.1 and Sect. 3.2, respectively. The method is developed and validated using the four SAR images overlapped with DMS DEM, see Fig. 2.

3.1 Sea ice classification

The random forest (RF) classifier (Breiman, 2001) is implemented to categorize sea ice, shown in Fig. 4, where SAR images and DMS DEM (h_{DMS}) are utilized as inputs into the proposed flowchart (Fig. 4). The penetration depth $h_{\mathrm{pene}} = h_{\mathrm{DMS}} - h_{\mathrm{InSAR}}$, where h_{DMS} measures the elevation from the snow-air surface relative to the seawater. InSAR DEM (h_{InSAR}) measures the elevation of the InSAR phase center, which can be somewhere inside of the snow or ice, depending on the snow and ice condition. h_{InSAR} is generated from TanDEM-X InSAR pair following the principles in Sect. 2.5. In general, microwaves can penetrate much shallower into the younger and more saline compared to the older and less saline sea ice (Hallikainen and Winebrenner, 1992). Hence, pixels with $h_{\mathrm{pene}} < 0.3\,\mathrm{m}$ are labeled as YI, whereas those with $h_{\mathrm{pene}} \leq 0.3\,\mathrm{m}$ are OI.
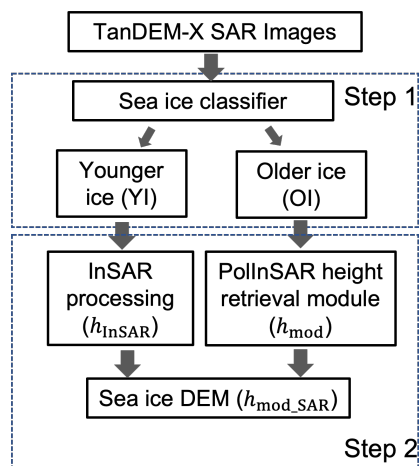
Figure 3. The proposed two-step approach for sea ice DEM retrieval. The details of the sea ice classifier and the PolInSAR height retrieval module are illustrated in Fig. 4 and 7, respectively.
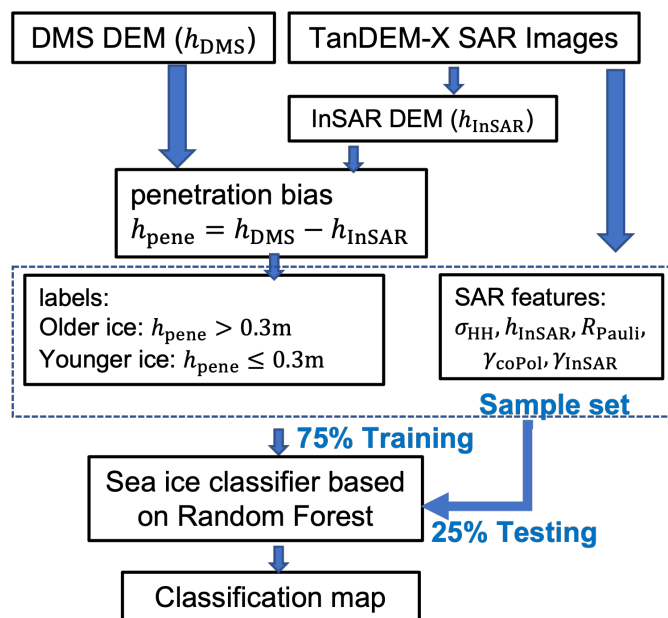
Figure 4. Flowchart for sea ice classification.
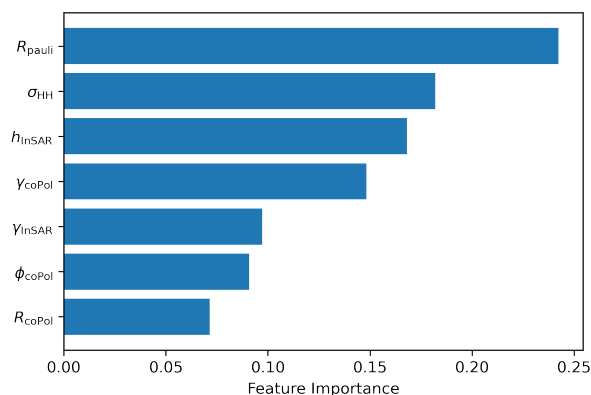
Figure 5. Gini importance computed from the Random Forest (RF) classifier.

We investigate a range of features for classification, including denoised backscattering intensity in HH polarization (σ_{HH}), polarimetric features such as coPol ratio (R_{coPol}), Pauli-polarization ratio (R_{Pauli}), coPol coherence magnitude (γ_{coPol}), and coPol phase (ϕ_{coPol}), as well as interferometric features including InSAR coherence magnitude (γ_{InSAR}) and height of interferometric phase center (h_{InSAR}). To improve computational performance, we rank features based on Gini Importance (i.e., Mean Decrease in Impurity), which measures the average gain of purity by splits of a given variable. The ranking of the features is illustrated in Fig. 5, where the top five features, i.e., R_{Pauli}, σ_{HH}, h_{InSAR}, γ_{coPol}, and γ_{InSAR} are selected as effective predictors for the RF classifier.

The selected features together with the ice labels (i.e., OI and YI) form the sample set. 75% is used for training the RF classifier, implemented in Python using default hyperparameters. Since sample numbers for the YI and OI classes are well-balanced (48% and 52%, respectively), no balanced training strategy is particularly implemented. The validation of ice classification over the testing subset (25%) will be given in Sect. 4.1.

3.2 DEM generation

Based on the classification map, we separately retrieve the sea ice elevations for the two categories of ice. For YI, the conventional InSAR processing (Section 2.5) is conducted, given the minimal penetration depth attributed to the saline ice. On the other hand, for OI which is subject to radar signal penetration, we apply the TLPV model developed in (Huang et al., 2021), which incorporates InSAR processing and corrects for the radar penetration bias into the snow-covered old ice. The TLPV model includes surface scattering from the top and bottom interfaces and volumes scattering from the snow and ice, shown in Fig. 6. The model was further simplified by merging the contributions of the snow volume, the ice volume, and the top layer
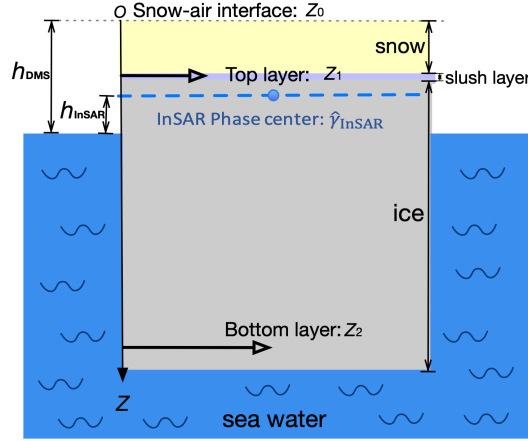
Figure 6. The schematic of the proposed TLPV model for sea ice (Huang et al., 2021).

into one Dirac delta (Huang et al., 2021):

$$
\begin{aligned}
\tilde{\gamma}_{\text{InSAR}} \\
&\approx e^{i\phi_0} \frac{1 \cdot e^{i\phi_1} + m \cdot e^{i\phi_2}}{1+m} \\
&= e^{i\phi_0} \tilde{\gamma}_{\text{mod}}(m, z_1, z_2) \\
&= e^{i\phi_0} \tilde{\gamma}_{\text{mod}}(m, z_1, h_v)
\end{aligned}
\tag{8}
$$

where ϕ_0 is the topographic phase at the snow-air interface, m refers to the layer-to-layer ratio, $\phi_1 = \kappa_{z\_\text{vol}} z_1$, $\phi_2 = \kappa_{z\_\text{vol}} z_2$, z_1 and z_2 are the locations of the layers, respectively. $h_v = z_1 - z_2$ refers to the depth between the top and bottom layer. κ_{z_vol}

195 is the vertical wavenumber in the volume which depends on the InSAR configuration such as HoA and the incidence angle, and the dielectric constant of the volume (Dall, 2007; Sharma et al., 2012; Huang et al., 2021).

The aim is to estimate ϕ_0 and convert it into height (h_{mod}). When fixing the origin at the air-snow interface, z_1 is equivalent to snow depth, which can be obtained from the AMSR Level-3 data (Meier, W. N., T. Markus, and J. C. Comiso, 2018). However, Eq. (8) still contains two unknown variables, m and h_v, preventing direct estimation of ϕ_0.

200 To address the above issue, we develop a new algorithm to invert the TLPV model and estimate m and h_v from SAR observations using RF regression, illustrated in Fig. 7. The RF regressor is trained using the same sample set as the sea ice classification. h_{DMS} can be transformed into ϕ_{DMS} by Eq. (3) and input as a priori information. With the above specific parameters, m and h_v values can be derived by inverting Eq. (8).

We also use Gini Importance to rank the seven features for regression, selecting the top five predictors for estimating m and

205 h_v: σ_{HH}, h_{InSAR}, γ_{InSAR}, R_{Pauli}, and ϕ_{coPol}, shown in Fig. 8. The selected features, together with the derived m and h_v, form the sample set that is partitioned into training (75%) and testing subsets (25%).

The selected features from InSAR observations, along with z_1 from ancillary data, are input into the well-trained RF regression model to estimate $\hat{m}$ and $\hat{h}_v$ over the testing set. Then the topographic phase $\hat{\phi}_0$ can be derived by solving Eq. (8), and
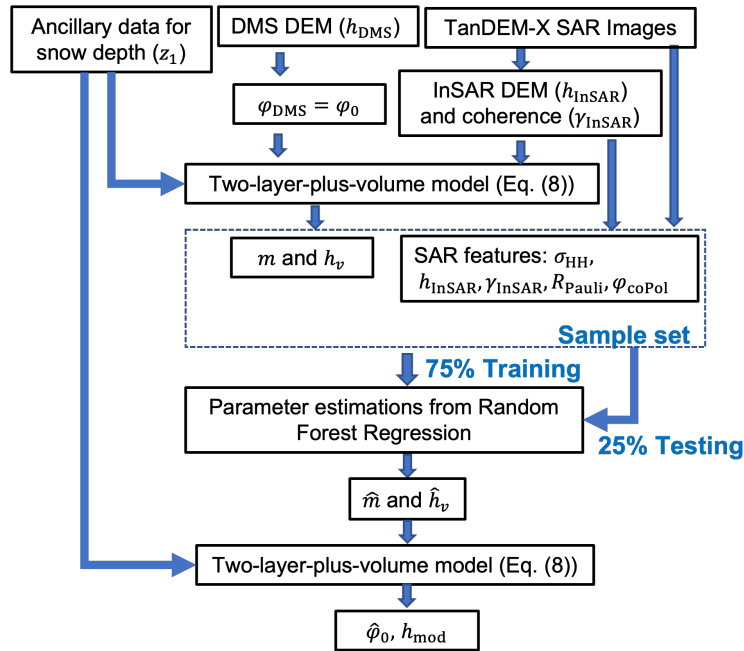
Figure 7. PolInSAR height retrieval module.

tranformed into elevation h_{mod} by Eq. (3). The validation of height retrieval accuracy over the testing subset (25%) will be given in the next section.

4   Results

Following the two-step approach developed in Sect. 3, this section obtains the SAR-derived DEM from 162 dual-pol InSAR pairs that cover the sea ice in the Weddell and Ross Seas. We verify the accuracy of the SAR-derived DEM. We further analyze the variation of elevation and roughness along the southward direction and examine the statistical characteristics of sea ice elevation across various geographic regions.

4.1   Sea ice topography retrieval and validation

The proposed two-step approach for sea ice elevation retrieval is visually and quantitatively validated based on the four scenes overlapped with DMS measurements. The SAR backscattering intensities over the four scenes are displayed in the left column in Fig. 9. In the first step, the proposed classification scheme (Fig. 4) demonstrates good performance on the testing set, with an accuracy of 0.84 and a confusion matrix presented in Fig. 10(a). The classifier is then applied to the entire SAR images, including the region not overlapped by DMS DEM, and the classified maps are shown in the middle column of Fig. 9.

In the second step, the sea ice DEM ($h_{\mathrm{mod\_SAR}}$) is obtained by merging h_{mod} and h_{InSAR} over OI and YI. The retrieved sea ice elevations are compared with h_{DMS} over the testing set, shown in Fig. 10(b). The RMSE between h_{InSAR} and h_{DMS} is
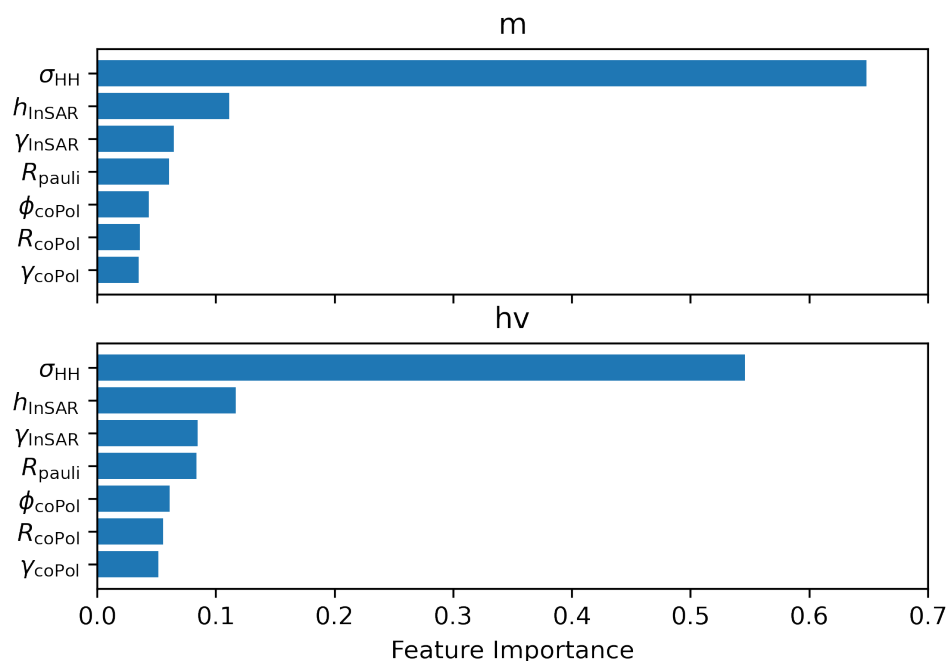
Figure 8. Gini importance computed from the Random Forest (RF) regressor for estimating m and h_v.

$0.18\,\mathrm{m}$, demonstrating good accuracy of applying conventional InSAR processing to retrieve sea ice DEM for YI. Regarding

225 OI, the proposed PolInSAR height retrieval module effectively compensates for the penetration bias, resulting in an RMSE of $0.25\,\mathrm{m}$ between h_{mod} and h_{DMS}. Note that the average RMSE value of OI without compensating the penetration bias is $\sim 1.10\,\mathrm{m}$ (Huang et al., 2021). When considering both types of ice, the RMSE between $h_{\mathrm{mod\_SAR}}$ and h_{DMS} is $0.26\,\mathrm{m}$. This result is promising as Dierking et al. (2017) suggested the satisfactory accuracy for a sea ice DEM being less than $0.3\,\mathrm{m}$.

The $h_{\mathrm{mod\_SAR}}$ over the entire SAR images are displayed in the right column of Fig. 9. For each scene, the white dash line

230 delineates a $50\,\mathrm{km} \times 100\,\mathrm{m}$ strip overlapped with DMS DEM. By extracting the values at the center of the strip, the height profiles are presented in Fig. 11, where $h_{\mathrm{mod\_SAR}}$ performs good agreement with the reference data (h_{DMS}) and well capture the topographic variation. Considering that h_{DMS} already contains an uncertainty of $0.2\,\mathrm{m}$ (Dotson and Arvesen., 2012, updated 2014), these results prove the effectiveness of the proposed two-step approach for sea ice DEM retrieval over both YI and OI.

4.2 Sea ice topography along the southwards direction

235 We obtain sea ice DEM over the 162 images using the two-step approach, shown in Fig. 12. The derived DEM is downsampled to a resolution of $500\,\mathrm{m}$, utilized in the subsequent analyses.

The northernmost location on each segment is selected and marked in Fig. 12. Subsequently, we characterize the variation of sea ice category, elevation, and roughness moving southward, using distances relative to the northernmost locations and
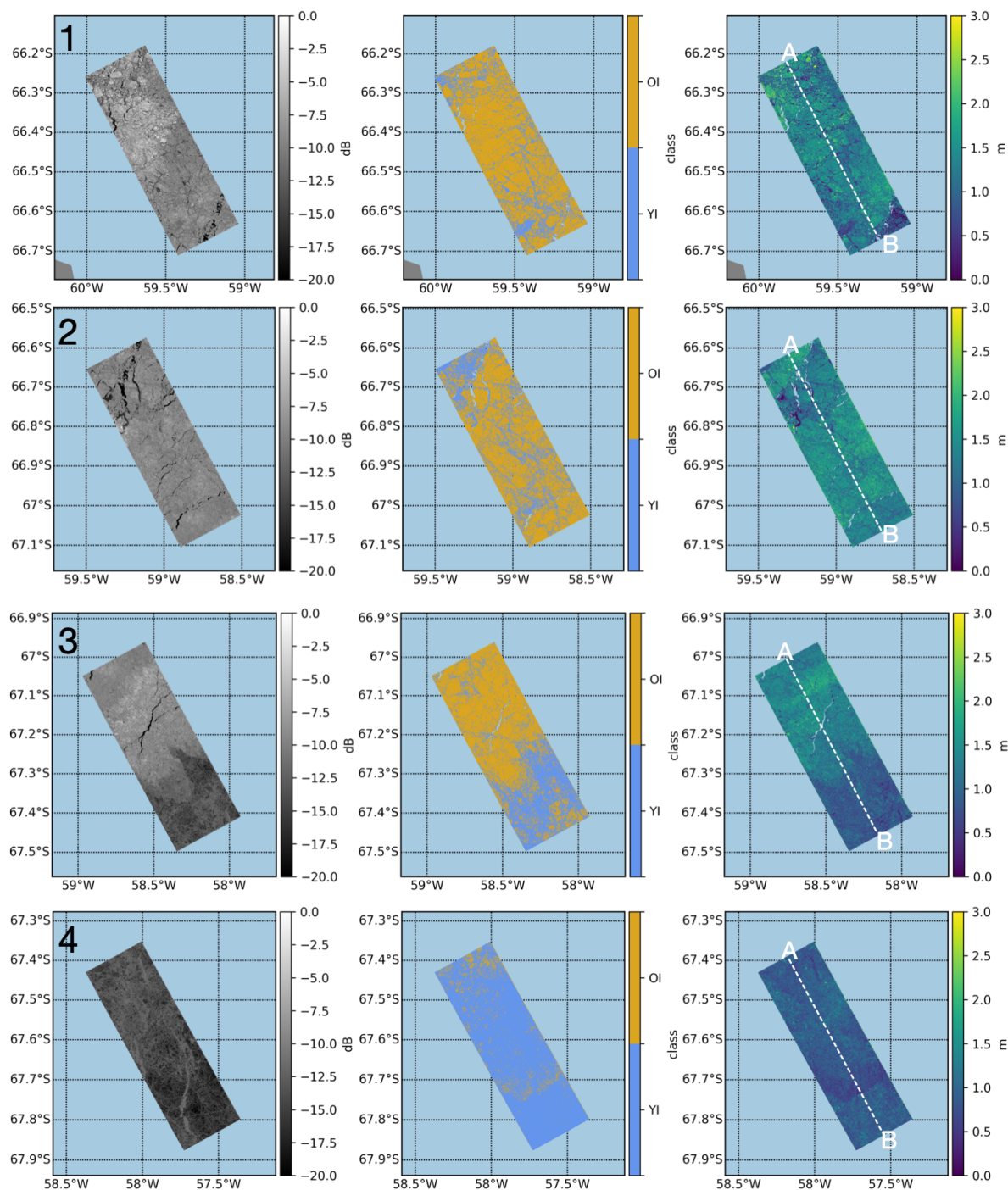
Figure 9. (a) SAR backscattering intensity in HH polarization, (b) sea ice classification, and (c) sea ice DEM ($h_{\mathrm{mod\_SAR}}$) over the four scenarios. Each row corresponds to Scene No.1-4 in Fig. 2, respectively. The white dashed line indicates the flight track overlapped by the DEM DEM (h_{DMS}).
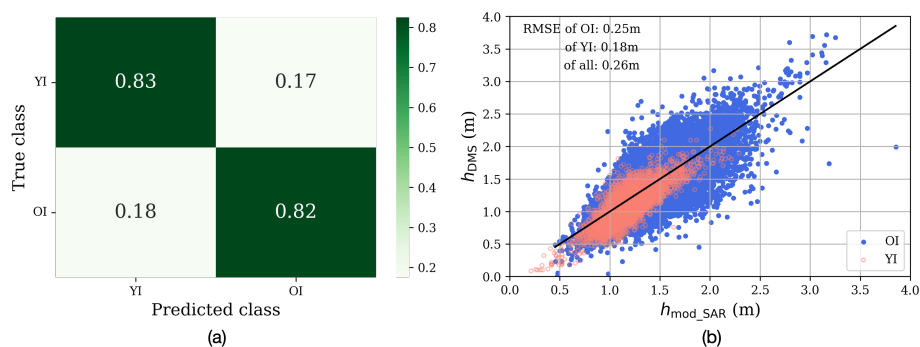
Figure 10. (a) Confusion matrix for sea ice classification. (b) Comparison between the reference height and the derived height over OI and YI.

averaging over every $100 \, \mathrm{km}$ interval. These topographic variations along the distance are illustrated in Fig. 13- 15. The first

240 column shows the OI percentages estimated from the proposed two-step approach and compared with the Ice Charts, which are used as the reference. For instance, the average ice type of the W1-U segment is MYI within the $0 - 160 \, \mathrm{km}$ range, matching the estimated around 58% OI from our method. FYI becomes dominant from $160 - 320 \, \mathrm{km}$, aligning with a decrease in OI percentage. Beyond $320 \, \mathrm{km}$, MYI dominates again, consistent with an increase in the estimated OI percentage.

The overall trend of estimated OI percentages aligns well with the Ice Charts across most segments (W1-U, W1-L, W2-U,

245 W4, W5-U, W5-L, and R5). For other segments, some discrepancies exist, which can be attributed to the differences in spatial resolution and temporal gap between the Ice Charts and SAR imagery, considering the dynamic nature of sea ice. It should be emphasized that the proposed method classifies ice based on electromagnetic wave penetration into snow and ice, which may have differences when compared with the conventional ice types in Ice Charts.

The second and third columns in Fig. 13- 15 display the distance dependency of ice elevation ($h_{\mathrm{mod_{SAR}}}$) and roughness (σ_R),

250 respectively. Sea ice roughness is the standard deviation of the elevation within a $50 \times 50 \, \mathrm{m}$ area. For each $100 \, \mathrm{km}$-distance interval, we calculate and display the average and median values, as well as the first and third quartiles of $h_{\mathrm{mod_{SAR}}}$ and σ_R using boxplots.

The Ice Charts are also used to validate and explain the topographic variation of sea ice. In general, the region with thicker ice (e.g., MYI) is anticipated to display higher elevation or larger roughness compared to the area with thinner ice, such as

255 FYI and TI. This hypothesis is substantiated by the agreement between topographical variations (elevation and roughness) and ice types observed in Fig. 13 to 15 across most segments, with the exception of W3-L and W5-L. The sea ice is identified as MYI between $450 - 750 \, \mathrm{km}$ in W3-L and $650 - 1000 \, \mathrm{km}$ in W5-L. However, neither elevation nor roughness significantly increases within these specific ranges. Minor discrepancies also persist, for instance, in W1-U and W2-L, where there is no clear reduction in either elevation or roughness when FYI is present at $600 \, \mathrm{km}$. Considering that the Ice Charts data are weekly

260 average, the inconsistencies could be attributed to mis-coregistration caused by sea ice drift during the time lag between the Ice Charts data and the SAR images.
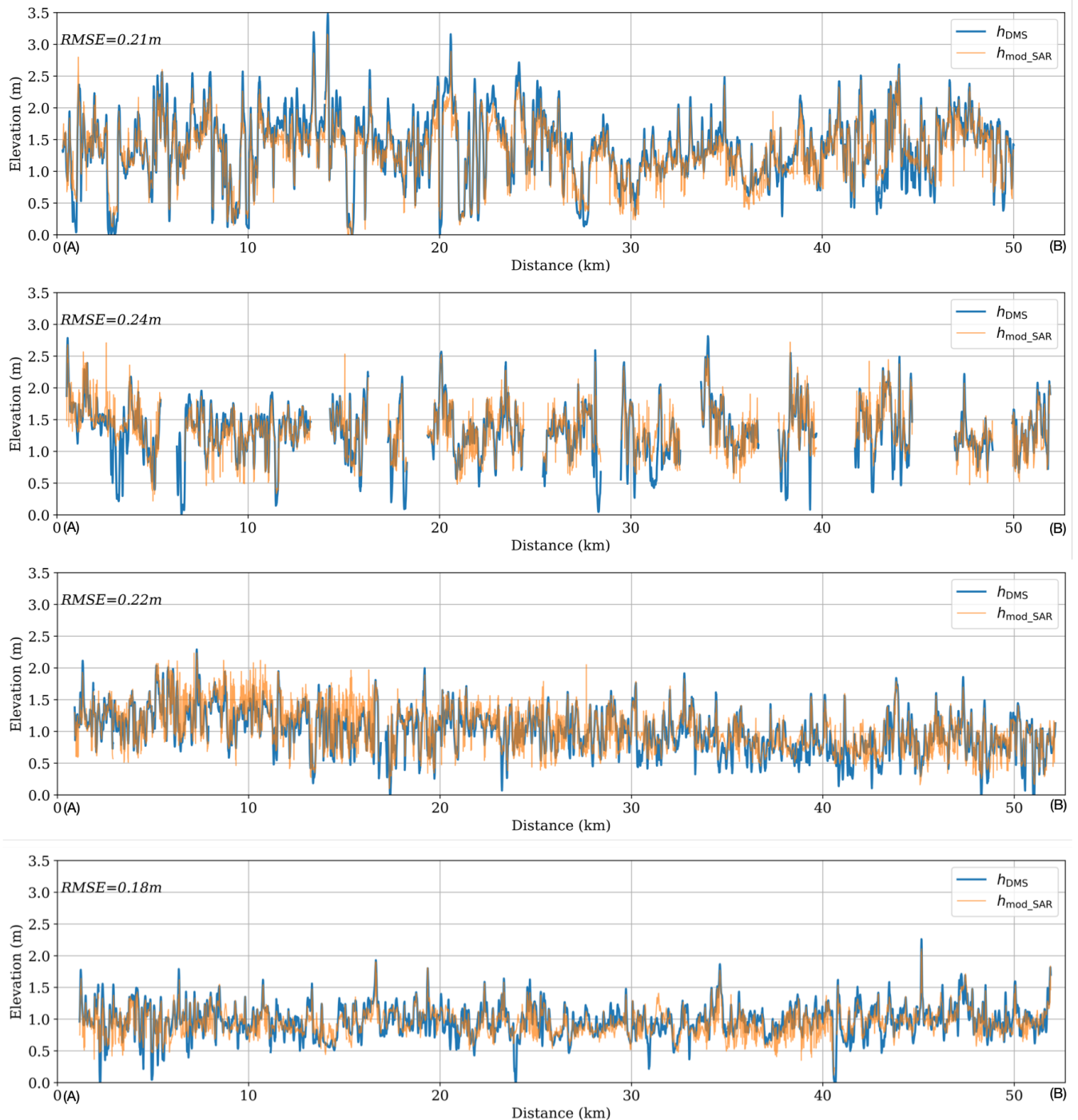
Figure 11. Comparison between the elevation profiles ($h_{\mathrm{mod\_SAR}}$) from the proposed method and the DMS DEM (h_{DMS}) along the dotted line (from A to B) over Scene No.1-4 in Fig. 9(c).
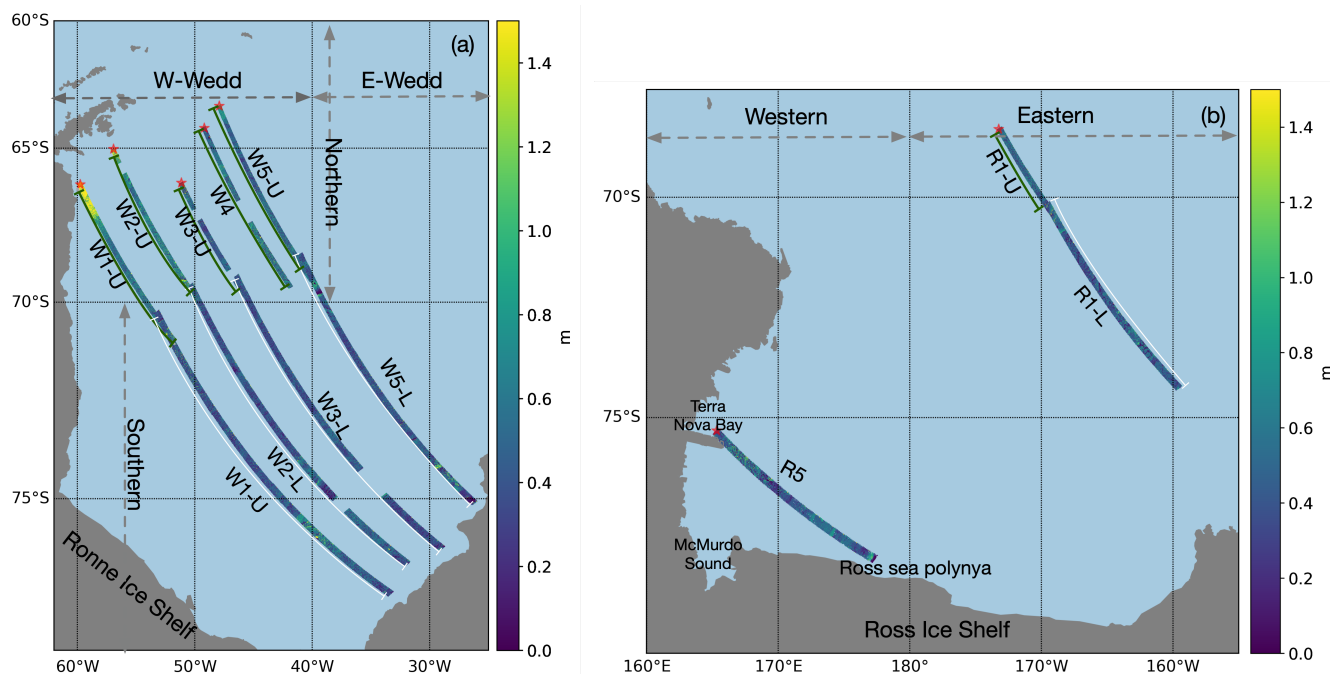
Figure 12. Sea ice DEM ($h_{\mathrm{mod\_SAR}}$) over (a) the Weddell Sea and (b) the Ross Sea retrieved from SAR images. The northernmost locations on each segment are marked with star symbols and serve as reference points for calculating the relative distance.

In the northwestern Weddell Sea, we observe that the sea ice near the Antarctic Peninsula (AP) in the W1-U and W2-U segments exhibits the highest average elevation (mean $> 0.7\,\mathrm{m}$) and roughness (mean $0.19\,\mathrm{m}$), shown in the first and third rows in Fig. 13. This observation aligns with a previous study using OIB Airborne Topographic Mapper (ATM) data from

265 November 14 and 22, 2017 (Wang et al., 2020), which has reported that the snow freeboard near the eastern AP ranges from $1.5 - 2.5\,\mathrm{m}$. Moving outwards from the AP, the sea ice elevation and roughness along W1-U and W2-U demonstrate a sharp decrease within approximately $0 - 200\,\mathrm{km}$ before gradually increasing as it heads southward. Similar trends are observed in W3-U (first row in Fig. 14) and W5-U (first row in Fig. 15), with a more subtle decrease in elevation and roughness within the $0 - 200\,\mathrm{km}$ range, compared to W1-U and W2-U, followed by a southward increase. Conversely, in the initial $0 - 200\,\mathrm{km}$

270 of W4 (third row in Fig. 14), there's no observed decrease in elevation or roughness. Instead, a gradual increase in both parameters is evident as one moves southward, consistent with the dominance of MYI beyond $100\,\mathrm{km}$ from the Ice Charts data. In the southeastern region, segments W1-L, W2-L, W3-L, and W5-L exhibit similar patterns in the topographic variation, with elevation and roughness generally decreasing towards the south as they approach the Coats Land. This trend can be explained by the increasing occurrence of FYI or TI beyond $\sim 1200\,\mathrm{km}$ from the Ice Charts data.

275 The observed variation in sea ice topography can result from the formation and dynamics of sea ice in the East Weddell (E-Wedd) and West Weddell (W-Wedd) regions, which are defined by specific longitude ranges: E-Wedd encompasses $15°\mathrm{E}$ to $40°\mathrm{W}$, while W-Wedd extends from $40°\mathrm{W}$ to $62°\mathrm{W}$. Segments of W1-U, W2-U, W3-U, W4, and W5-U are located within the
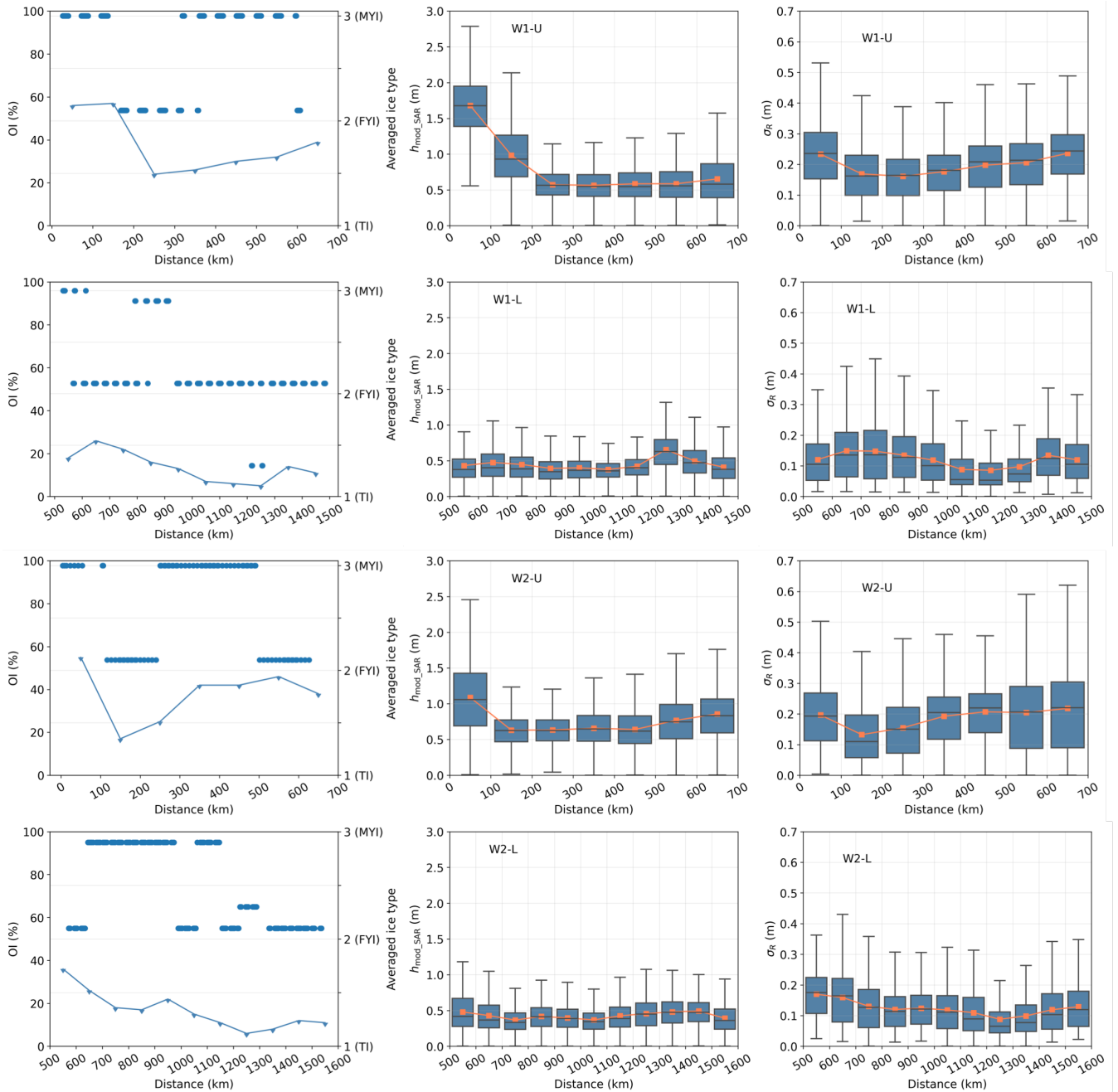
Figure 13. Sea ice characteristics along the southwards direction along W1 and W2 segments. The blue line in the first column displays the OI percentages derived from SAR images, and the blue dot indicates the ice types obtained from the Ice Charts. The second and third columns plot the elevation ($h_{\mathrm{mod\_SAR}}$) and roughness (σ_R), respectively. Distance is measured from the northernmost SAR image reference point towards the south. The orange line denotes the average values of $h_{\mathrm{mod_SAR}}$ and σ_R. The box's upper and lower boundaries represent the first (Q1) and third (Q3) quartiles, while the upper (lower) whisker extends to the last (first) sample outside of Q3 ±1.5×(Q3-Q1).
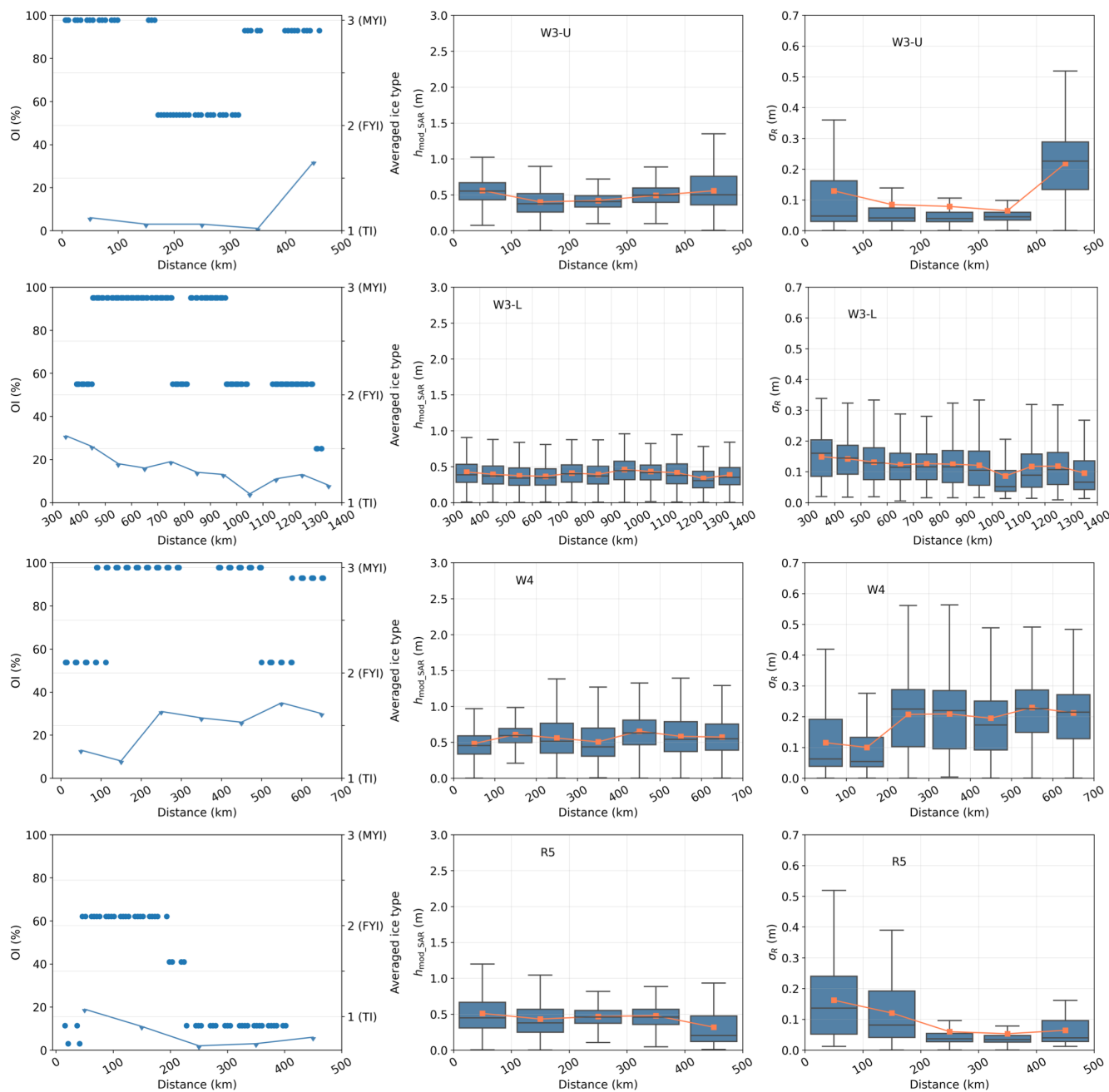
Figure 14. Sea ice characteristics along the southwards direction along W3, W4, and R5 segments. The blue line in the first column displays the OI percentages derived from SAR images, and the blue dot indicates the ice types obtained from the Ice Charts. The second and third columns plot the elevation ($h_{\mathrm{mod\_SAR}}$) and roughness (σ_R), respectively.
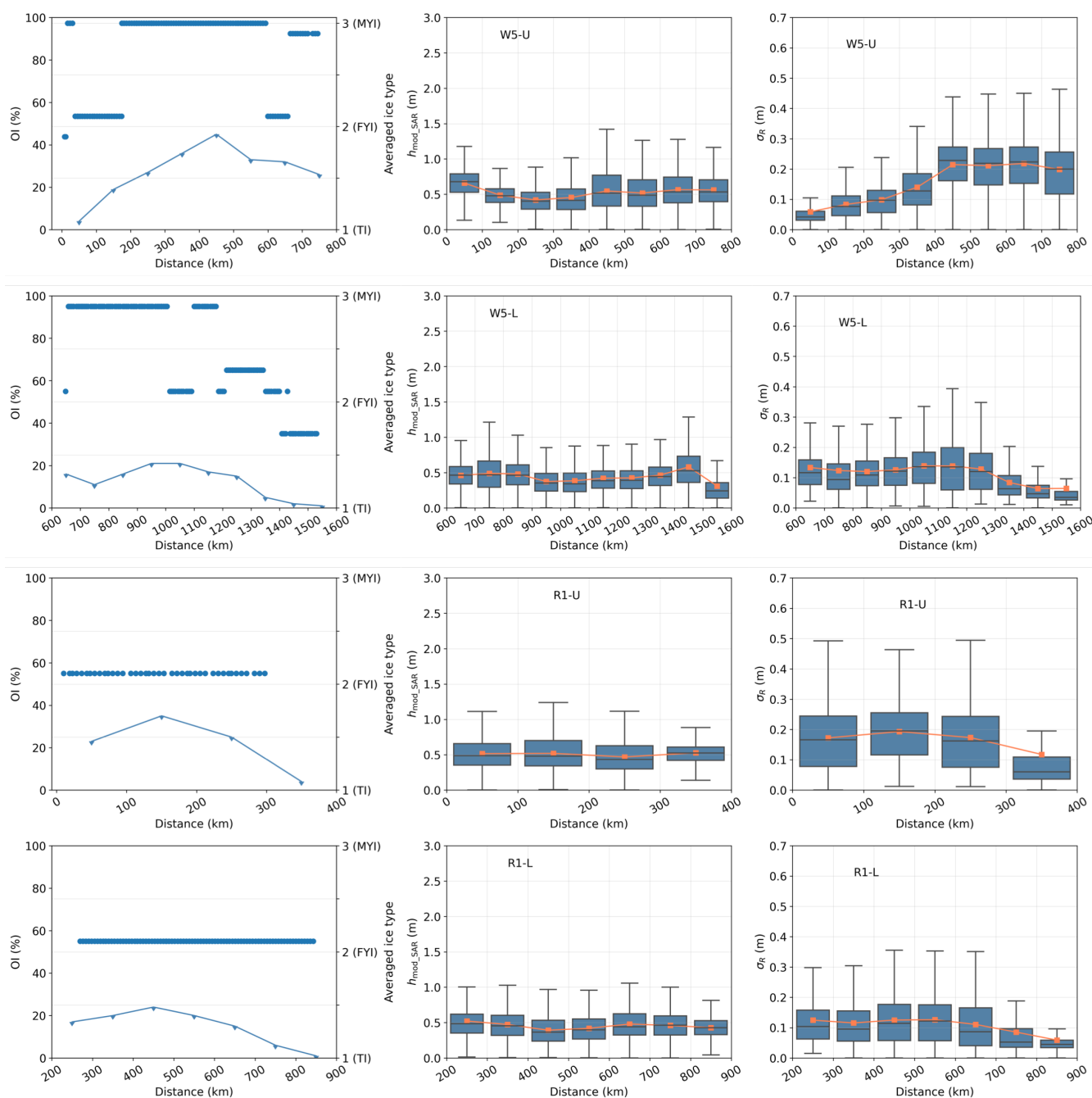
Figure 15. Sea ice characteristics along the southwards direction along W5 and R1 segments. The blue line in the first column displays the OI percentages derived from SAR images, and the blue dot indicates the ice types obtained from the Ice Charts. The second and third columns plot the elevation ($h_{\mathrm{mod\_SAR}}$) and roughness (σ_R), respectively.

W-Wedd, which has been reported for the presence of MYI in the Antarctic (Lange and Eicken, 1991). Sea ice initially forms in the eastern region and then circulates clockwise within the cyclonic gyre of the southern Weddell Sea. Later, older sea ice drifts outward northwestern (Kacimi and Kwok, 2020). The sea ice undergoes thickening and deformation as it drifts (Vernet et al., 2019; Kacimi and Kwok, 2020), resulting in increased elevation and greater roughness in the northwestern Weddell Sea.

In the Western Ross Sea, the sea ice in the R5 segment (last row in Fig. 14) exhibits greater elevation and roughness near Terra Nova Bay, with decreasing southeastward. This observation aligns with the evolution of ice types from MTI to TI in that direction. This observation is also consistent with recent research (Rack et al., 2021), where airborne measurements in November 2017 revealed deformed sea ice exceeding $10\,\mathrm{m}$ in thickness within the first $100\,\mathrm{km}$ south of Terra Nova Bay, and thinner ice was observed towards the southeastern area near McMurdo Sound (see Fig. 12b for the location). Satellite data also confirmed a region of thinner ice influenced by the Ross Sea Polynya, with thicker ice located westward (Kurtz and Markus, 2012). The observed pattern can be attributed to significant deformation in the Western Ross Sea caused by wind-driven shearing, rafting, and ridging within a convergent sea ice regime (Hollands and Dierking, 2016). This deformation leads to potentially thicker sea ice compared to the eastern part (Rack et al., 2021).

For the R1 segment located in the Eastern Ross Sea (third and fourth rows in Fig. 15), although the sea ice exhibits relatively stable elevation, which agrees with the consistent presence of predominantly FYI, the roughness decreases towards the southeastern. This may be attributed to the influence of ocean circulation, considering that the R1 segment is situated farther from the land than the other segments. The variation of the roughness along the R1 segment also highlights the importance of combining topographic mapping with ice category mapping to comprehensively characterize sea ice features.

4.3 Regional variation of sea ice topography

Figure 16(a) displays the topographic variation across different segments. We present the average and median values, as well as the first and third quartiles of elevation and roughness using boxplots. The mean values are listed in Table 3. Additionally, the percentages of the three ice types within each segment, calculated from the Ice Charts for reference, are presented in Fig. 16(b).

Generally, sea ice in the northwestern Weddell Sea (W1-U, W2-U, W3-U, W4, W5-U) exhibits higher average elevations ($> 0.5\,\mathrm{m}$) compared to that in the southeastern Weddell Sea and the Ross Sea (W1-L, W2-L, W3-L, W5-L, R1-U, R1-L, R5), see detailed values in Table 3. W1-U and W2-U exhibit the highest average elevations of $0.8\,\mathrm{m}$ and $0.72\,\mathrm{m}$, respectively, along with the largest average roughness of $0.19\,\mathrm{m}$. This is comparable with the snow freeboard retrieved from ICESat-2 (Kacimi and Kwok, 2020), reporting an average of $0.6 - 0.7\,\mathrm{m}$ snow freeboard nearby the Eastern AP between April 1 and November 16, 2019. W4 and W5-U show average elevations of $0.57\,\mathrm{m}$ and $0.52\,\mathrm{m}$, and average roughness values of $0.18\,\mathrm{m}$ and $0.16\,\mathrm{m}$, respectively. The above topographic values (i.e., elevation and roughness) are consistent with the ice types presented in Fig. 16(b), where W1-U, W2-U, W4, and W5-U exhibit a substantial proportion ($> 57\%$) of MYI, known for greater elevation and roughness characteristics. W3-U, which consists of 58% MYI, exhibits an elevation of $0.50\,\mathrm{m}$ but with relatively lower roughness at $0.11\,\mathrm{m}$, suggesting the possibility of a smooth snow-air interface over older and thicker ice.

For the segments in the southeastern Weddell Sea and the Ross Sea (W1-L, W2-L, W3-L, W5-L, R1-L, and R5), the average sea ice elevation remains below $0.46\,\mathrm{m}$ and roughness around $0.11\,\mathrm{m}$. The reduced average elevation and roughness correspond
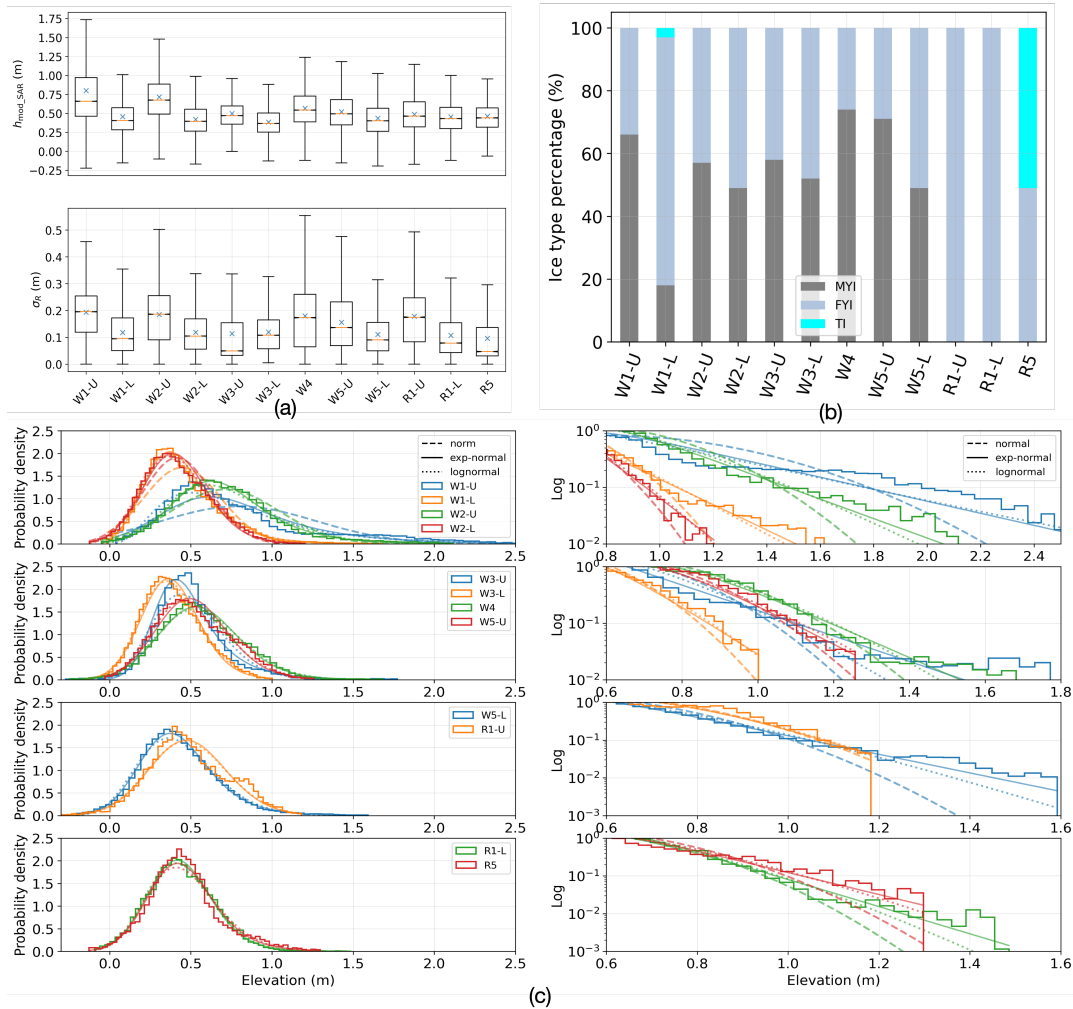
Figure 16. (a) Sea ice elevation ($h_{\text{mod\_SAR}}$) and roughness (σ_R) derived from SAR images across the 12 segments. (b) The percentage of multi-year ice (MYI), first-year ice (FYI), and thin ice (TI) from the Ice Charts. (c) Probability density function (PDF) of derived sea ice elevation ($h_{\text{mod}_{S}\text{AR}}$) and their fits to the exponential-normal, log-normal, and normal distributions.

to ice types with fewer MYI percentages ($<\sim 50\%$) and greater amounts of FYI and TI ($>\sim 50\%$). R1-U demonstrates an average sea ice elevation of $0.49\,\text{m}$ and roughness of $0.18\,\text{m}$, with the presence of predominantly FYI throughout the region. This observation suggests a plausible scenario of a rougher snow-air interface over younger and thinner ice (Tin and Jeffries, 2001; Tian et al., 2020).

315

Table 3. Average elevation and roughness for each segment, as well as the Kolmogorov-Smirnov (KS) values between the observed elevations and modeled distributions (i.e., exponential normal and log-normal). The smaller KS value is in **bold**.

segment	Mean elevation (m)	Mean roughness (m)	KS exp-normal	KS log-normal
W1-U	0.80	0.19	**0.083**	0.106
W1-L	0.46	0.12	0.064	**0.05**
W2-U	0.72	0.19	**0.052**	0.07
W2-L	0.42	0.12	0.079	**0.054**
W3-U	0.50	0.11	**0.113**	0.2
W3-L	0.39	0.12	0.065	**0.05**
W4	0.57	0.18	**0.035**	0.072
W5-U	0.52	0.16	**0.074**	0.076
W5-L	0.44	0.11	**0.038**	0.078
R1-U	0.49	0.18	0.053	**0.049**
R1-L	0.45	0.11	**0.049**	0.106
R5	0.46	0.10	0.052	**0.039**
Overall			**0.063**	0.079

4.4 Statistical analyses of sea ice topography

Studies on sea ice topography in the Arctic have extensively examined the applicability of statistical distributions such as the log-normal distribution (Landy et al., 2020; Duncan and Farrell, 2022) and the exponentially modified normal (exp-normal) distribution (Yi et al., 2022). However, there remains a gap in understanding the most suitable distribution models for describing the elevation of Antarctic sea ice. We aim to address this gap by evaluating three distribution models: Gaussian, log-normal, and exp-normal, to determine the most appropriate probability density function (PDF) for describing the sea-ice elevation across segments.

The PDF of the Gaussian distribution with mean μ_g and standard deviation σ_g is defined as:

$$G(x) = \frac{1}{\sqrt{2\pi\sigma_g^2}} e^{-\frac{(x-\mu_g)^2}{2\sigma_g^2}} \tag{9}$$

The PDF of the log-normal distribution with mean $e^{(\mu_l + \sigma_l^2/2)}$ and variance $e^{2\mu_l + \sigma_l^2}\left(e^{\sigma_l^2} - 1\right)$ follows (Gaddum, 1945):

$$LG(x) = \frac{1}{x\sigma_l\sqrt{2\pi}} e^{-\frac{(\ln(x)-\mu_l)^2}{2\sigma_l^2}} \tag{10}$$

The PDF of the exp-normal distribution with mean $\mu_e + 1/\lambda$ and variance $\sigma_e^2 + 1/\lambda^2$ is given as (Foley and Dorsey, 1984):

$$EMG(x) = \frac{\lambda}{2} e^{\frac{\lambda}{2}(2\mu_e + \lambda\sigma_e^2 - 2x)} \text{erfc}(\frac{\mu_e + \lambda\sigma_e^2 - x}{\sqrt{2}\sigma_e}) \tag{11}$$

where the erfc$(\cdot)$ is the complementary error function with erfc$(x) = \frac{2}{\sqrt{\pi}} \int_x^\infty e^{-t^2} \, dt$.

330   The observed and modeled distributions of sea ice elevation over each segment are depicted in the left column of Fig. 16(c). The observed distributions of all segments exhibit asymmetrical with longer tails. A closer examination of the tail regions (right column in Fig. 16(c)) reveals significant deviations from the Gaussian distribution, particularly in segments W1-U and W2-U, which are covered by deformed and thicker sea ice. The observed non-Gaussian nature of sea ice elevation distribution aligns with the previous studies (Hughes, 1991; Davis and Wadhams, 1995; Castellani et al., 2014; Landy et al., 2019; Huang
335   et al., 2021). To quantitatively evaluate the fit of non-Gaussian distributions (i.e., log-normal and exp-normal) to the observed elevations, we employ the Kolmogorov-Smirnov (KS) test (Massey Jr, 1951). This test measures the goodness of fitting by calculating the distance between the observed distribution function and the theoretical cumulative distribution function. The values of the KS test are given in Table 3, where a lower value indicates a better fit.

In the northwestern Weddell Sea, where the segments (W1-U, W2-U, W3-U, W4-U, and W5-U) have average elevations
340   greater than $0.5\,\mathrm{m}$, the exp-normal distribution demonstrates superior fitting performance, as evidenced by smaller KS values. This can be attributed to the exp-normal distribution's incorporation of an exponential component, which enables a better fit to data with heavy or long tails compared to the log-normal distribution. Consequently, the exp-normal distribution is better suited for characterizing the statistics of older and thicker sea ice, which often involves strong deformation and exhibits significant elevations.

345   In the southern Weddell Sea and the Ross Sea, segments average below $0.5\,\mathrm{m}$ in elevation, with varying fits between exp-normal and log-normal distributions. The log-normal distribution exhibits a better fit for W1-L, W2-L, W3-L, R1-U, and R5, while the exp-normal distribution is more appropriate for W5-L and R1-L. This observation suggests that the two distributions perform comparably in characterizing the elevations of younger and thinner sea ice.

Evaluating the overall performance across all segments, the exp-normal distribution outperforms the log-normal distribution,
350   as indicated by a smaller average KS value of 0.063.

5   Conclusions

In this study, we proposed a novel two-step approach integrating machine learning and polarimetric-interferometry techniques to retrieve sea ice elevation from dual-pol single-pass InSAR images, taking into account the variations in penetration bias over different ice classes. Initially, a random forest classifier was employed to categorize sea ice (i.e, YI and OI) based on
355   microwaves' penetration. Subsequently, the standard InSAR processing technique was applied to retrieve the elevation over YI regions, where the penetration depth is negligible. For OI regions, an inversion algorithm for the TLPV model was developed. This algorithm can effectively compensate for the radar penetration bias into snow and ice, achieving an accurate sea ice DEM (i.e., snow freeboard). Utilizing the OTASC dataset, which spans an area of $200 \times 19\,\mathrm{km}$, the efficiency of the proposed method was validated with an RMSE of $0.26\,\mathrm{m}$.

360   The proposed approach was applied to a broad area in Antarctica. Overall, sea ice in the northwestern Weddell Sea exhibits higher average elevations ($> 0.5\,\mathrm{m}$) than the southeastern region and the Ross Sea, where the average elevations are lower

($< 0.5\,\mathrm{m}$). In the northwestern Weddell Sea, sea ice experiences substantial deformation near the eastern AP, followed by a pronounced decline in both elevation and roughness within a range of $0 - 200\,\mathrm{km}$. Subsequently, there is a gradual increase in these parameters as one moves southward. In the southeastern Weddell Sea, the sea ice elevation and roughness generally

365 decrease towards the south as they approach Coats Land. In the Western Ross Sea, thicker and rougher ice was observed near Terra Nova Bay, while thinner ice was found in the southeastern area near McMurdo Sound. In the Eastern Ross Sea, the stable sea ice elevation aligns with the prevalent presence of FYI, but roughness decreases towards the southeastern. These findings emphasize that topographic mapping can enhance ice category delineation, providing an in-depth understanding of sea ice characteristics.

370 Furthermore, the statistical analyses of sea ice elevation confirmed its non-Gaussian distribution. The results further suggested that the exp-normal distribution outperforms the log-normal distribution in fitting the elevations of regions with an average elevation greater than $0.5\,\mathrm{m}$, particularly for older and thicker sea ice, whereas both distributions perform comparably for regions with an average elevation lower than $0.5\,\mathrm{m}$.

Future studies involve linking the derived sea ice topographic characteristics associated with oceanographic factors (ocean

375 current and bathymetry) and climatology parameters (wind and temperature). We aim to further advance our comprehension of sea ice dynamics and evolution in Antarctica.

Data availability. TanDEM-X imagery can be acquired from the German Aerospace Center (DLR) by submitting a scientific proposal, accessible at https://eoweb.dlr.de. Additionally, DMS data can be obtained from the National Snow and Ice Data Center at https://nsidc.org/data/icebridge, while Ice Charts data are available at https://nsidc.org/data/G10033/versions/1, also from the National Snow and Ice Data Center.

380 *Author contributions.* LH carried out SAR image processing, designed the methodology, analyzed the results, and drafted the manuscript. IH provided valuable input on method development and result analysis, contributing to the enhancement of the manuscript

Competing interests. The authors have no conflicts of interest to disclose.

Acknowledgements. The authors would like to thank all individuals involved in the OTASC campaign, jointly conducted by DLR and NASA. Special thanks are extended to Dr. Thomas Busche for his invaluable assistance in accessing the TanDEM-X data.

References

Breiman, L.: Random forests, Machine learning, 45, 5–32, https://doi.org/10.1023/A:1010933404324, 2001.

Castellani, G., Lüpkes, C., Hendricks, S., and Gerdes, R.: Variability of Arctic sea-ice topography and its impact on the atmospheric surface drag, J. Geophys. Res.: Oceans, 119, 6743–6762, https://doi.org/10.1002/2013JC009712, 2014.

Cloude, S.: Polarisation: applications in remote sensing, Oxford University Press, https://doi.org/10.1093/acprof:oso/9780199569731.001.0001, 2010.

Dall, J.: InSAR elevation bias caused by penetration into uniform volumes, IEEE Trans. Geosci. Remote Sens., 45, 2319–2324, https://doi.org/10.1109/TGRS.2007.896613, 2007.

Dammann, D. O., Eicken, H., Mahoney, A. R., Saiet, E., Meyer, F. J., John, C., et al.: Traversing sea ice—linking surface roughness and ice trafficability through SAR polarimetry and interferometry, IEEE J. Sel. Top. Appl. Earth Obs. Remote Sens., 11, 416–433, https://doi.org/10.1109/JSTARS.2017.2764961, 2017.

Davis, N. and Wadhams, P.: A statistical analysis of Arctic pressure ridge morphology, J. Geophys. Res.: Oceans, 100, 10 915–10 925, https://doi.org/10.1029/95JC00007, 1995.

Dierking, W.: Laser profiling of the ice surface topography during the Winter Weddell Gyre Study 1992, J. Geophys. Res.: Oceans, 100, 4807–4820, https://doi.org/10.1029/94JC01938, 1995.

Dierking, W., Lang, O., and Busche, T.: Sea ice local surface topography from single-pass satellite InSAR measurements: a feasibility study, The Cryosphere, 11, 1967–1985, https://doi.org/10.5194/tc-11-1967-2017, 2017.

Dominguez, R.: IceBridge DMS L1B geolocated and orthorectified Images, Version 1, Boulder, Colorado USA: NASA National Snow and Ice Data Center Distributed Active Archive Center, https://doi.org/10.5067/OZ6VNOPMPRJ0, accessed Nov 22, 2018., 2010, updated 2018.

Dotson, R. and Arvesen., J.: IceBridge DMS L3 photogrammetric DEM, version 1., Boulder, Colorado USA: NASA National Snow and Ice Data Center Distributed Active Archive Center, https://doi.org/10.5067/39YO5T544XCC, accessed Nov 22, 2018., 2012, updated 2014.

Duncan, K. and Farrell, S. L.: Determining Variability in Arctic Sea Ice Pressure Ridge Topography With ICESat-2, Geophys. Res. Lett., 49, e2022GL100 272, https://doi.org/10.1029/2022GL100272, 2022.

Foley, J. P. and Dorsey, J. G.: A review of the exponentially modified Gaussian (EMG) function: evaluation and subsequent calculation of universal data, J. Chromatogr. Sci., 22, 40–46, https://doi.org/10.1093/chromsci/22.1.40, 1984.

Gaddum, J. H.: Lognormal distributions, Nature, 156, 463–466, https://doi.org/10.1038/156463a0, 1945.

Garbrecht, T., Lüpkes, C., Hartmann, J., and Wolff, M.: Atmospheric drag coefficients over sea ice–validation of a parameterisation concept, Tellus A: Dynamic Meteorology and Oceanography, 54, 205–219, https://doi.org/10.3402/tellusa.v54i2.12129, 2002.

Guneriussen, T., Hogda, K. A., Johnsen, H., and Lauknes, I.: InSAR for estimation of changes in snow water equivalent of dry snow, IEEE Trans Geosci Remote Sens., 39, 2101–2108, https://doi.org/10.1109/36.957273, 2001.

Hallikainen, M. and Winebrenner, D. P.: The physical basis for sea ice remote sensing, Microwave remote sensing of sea ice, 68, 29–46, https://doi.org/10.1029/GM068p0029, 1992.

Hollands, T. and Dierking, W.: Dynamics of the Terra Nova Bay Polynya: The potential of multi-sensor satellite observations, Remote Sens. Environ., 187, 30–48, https://doi.org/10.1016/j.rse.2016.10.003, 2016.

Huang, L. and Hajnsek, I.: Polarimetric Behavior for the Derivation of Sea Ice Topographic Height From TanDEM-X Interferometric SAR Data, IEEE J. Sel. Top. Appl. Earth Obs. Remote Sens., 14, 1095–1110, https://doi.org/10.1109/JSTARS.2020.3036395, 2021.

Huang, L., Fischer, G., and Hajnsek, I.: Antarctic snow-covered sea ice topography derivation from TanDEM-X using polarimetric SAR interferometry, The Cryosphere, 15, 5323–5344, https://doi.org/10.5194/tc-15-5323-2021, 2021.

Huang, L., Hajnsek, I., and Nghiem, S. V.: Sea ice elevation in the Western Weddell Sea, Antarctica: Observations from field campaign,
425 Earth Space Sci., 9, e2022EA002 472, https://doi.org/10.1029/2022EA002472, 2022.

Hughes, B.: On the use of lognormal statistics to simulate one-and two-dimensional under-ice draft profiles, J. Geophys. Res.: Oceans, 96, 22 101–22 111, https://doi.org/10.1029/91JC02336, 1991.

Kacimi, S. and Kwok, R.: The Antarctic sea ice cover from ICESat-2 and CryoSat-2: freeboard, snow depth, and ice thickness, The Cryosphere, 14, 4453–4474, https://doi.org/10.5194/tc-14-4453-2020, 2020.

Kim, J.-W., Kim, D.-j., and Hwang, B. J.: Characterization of Arctic sea ice thickness using high-resolution spaceborne polarimetric SAR
430 data, IEEE Trans. Geosci. Remote Sens., 50, 13–22, https://doi.org/10.1109/TGRS.2011.2160070, 2011.

Krieger, G., Moreira, A., Fiedler, H., Hajnsek, I., Werner, M., Younis, M., and Zink, M.: TanDEM-X: A satellite formation for high-resolution SAR interferometry, IEEE Trans. Geosci. Remote Sens., 45, 3317–3341, https://doi.org/10.1109/TGRS.2007.900693, 2007.

Kurtz, N. T. and Markus, T.: Satellite observations of Antarctic sea ice thickness and volume, J. Geophys. Res.: Oceans, 117,
435 https://doi.org/10.1029/2012JC008141, 2012.

Kwok, R. and Kacimi, S.: Three years of sea ice freeboard, snow depth, and ice thickness of the Weddell Sea from Operation IceBridge and CryoSat-2, The Cryosphere, 12, 2789–2801, https://doi.org/10.5194/tc-12-2789-2018, 2018.

Landy, J. C., Tsamados, M., and Scharien, R. K.: A facet-based numerical model for simulating SAR altimeter echoes from heterogeneous sea ice surfaces, IEEE Transactions on Geoscience and Remote Sensing, 57, 4164–4180, https://doi.org/10.1109/TGRS.2018.2889763,
440 2019.

Landy, J. C., Petty, A. A., Tsamados, M., and Stroeve, J. C.: Sea ice roughness overlooked as a key source of uncertainty in CryoSat-2 ice freeboard retrievals, J. Geophys. Res.: Oceans, 125, e2019JC015 820, https://doi.org/10.1029/90JC02441, 2020.

Lange, M. and Eicken, H.: The sea ice thickness distribution in the northwestern Weddell Sea, J. Geophys. Res.: Oceans, 96, 4821–4837, 1991.

445 Lee, J.-S. and Pottier, E.: Polarimetric radar imaging: from basics to applications, CRC press, 2009.

Leinss, S., Parrella, G., and Hajnsek, I.: Snow height determination by polarimetric phase differences in X-band SAR data, IEEE J. Sel. Top. Appl. Earth Obs. Remote Sens., 7, 3794–3810, https://doi.org/10.1109/JSTARS.2014.2323199, 2014.

Leinss, S., Löwe, H., Proksch, M., Lemmetyinen, J., Wiesmann, A., and Hajnsek, I.: Anisotropy of seasonal snow measured by polarimetric phase differences in radar time series, The Cryosphere, 10, 1771–1797, https://doi.org/10.5194/tc-10-1771-2016, 2016.

450 Massey Jr, F. J.: The Kolmogorov-Smirnov test for goodness of fit, Journal of the American statistical Association, 46, 68–78, https://doi.org/10.1080/01621459.1951.10500769, 1951.

Massom, R. A., Eicken, H., Hass, C., Jeffries, M. O., Drinkwater, M. R., Sturm, M., Worby, A. P., Wu, X., Lytle, V. I., Ushio, S., et al.: Snow on Antarctic sea ice, Rev. Geophys., 39, 413–445, https://doi.org/10.1029/2000RG000085, 2001.

Meier, W. N., T. Markus, and J. C. Comiso: AMSR-E/AMSR2 Unified L3 Daily 12.5 km Brightness Temperatures, Sea Ice Concentration,
455 Motion & Snow Depth Polar Grids, Version 1, Boulder, Colorado USA: NASA National Snow and Ice Data Center Distributed Active Archive Center, https://doi.org/10.5067/RA1MIJOYPK3P. Accessed Jan 23, 2021., 2018.

Nghiem, S., Kwok, R., Yueh, S., and Drinkwater, M.: Polarimetric signatures of sea ice: 2. Experimental observations, J. Geophys. Res.: Oceans, 100, 13 681–13 698, https://doi.org/10.1080/08843759508947700, 1995.

Nghiem, S., Busche, T., Kraus, T., Bachmann, M., Kurtz, N., Sonntag, J., Woods, J., Ackley, S., Xie, H., Maksym, T., et al.: Remote
Sensing of Antarctic Sea Ice with Coordinated Aircraft and Satellite Data Acquisitions, in: IGARSS 2018, pp. 8531–8534, IEEE,
https://doi.org/10.1109/IGARSS.2018.8518550, 2018.

Nghiem, S. V., Huang, L., and Hajnsek, I.: Theory of radar polarimetric interferometry and its application to the retrieval of sea ice elevation
in the Western Weddell Sea, Antarctic, Earth Space Sci., 9, e2021EA002 191, https://doi.org/10.1029/2021EA002191, 2022.

Petty, A. A., Tsamados, M. C., Kurtz, N. T., Farrell, S. L., Newman, T., Harbeck, J. P., Feltham, D. L., and Richter-Menge, J. A.: Charac-
terizing Arctic sea ice topography using high-resolution IceBridge data, The Cryosphere, 10, 1161–1179, https://doi.org/10.5194/tc-10-
1161-2016, 2016.

Rack, W., Price, D., Haas, C., Langhorne, P. J., and Leonard, G. H.: Sea ice thickness in the Western Ross Sea, Geophys. Res. Lett., 48,
e2020GL090 866, https://doi.org/10.1029/2020GL090866, 2021.

Ressel, R., Singha, S., Lehner, S., Rösel, A., and Spreen, G.: Investigation into different polarimetric features for sea ice
classification using X-band synthetic aperture radar, IEEE J. Sel. Top. Appl. Earth Obs. Remote Sens., 9, 3131–3143,
https://doi.org/10.1109/JSTARS.2016.2539501, 2016.

Sharma, J. J., Hajnsek, I., Papathanassiou, K. P., and Moreira, A.: Estimation of glacier ice extinction using long-wavelength airborne Pol-
InSAR, IEEE Trans. Geosci. Remote Sens., 51, 3715–3732, https://doi.org/10.1109/TGRS.2012.2220855, 2012.

Singha, S., Johansson, M., Hughes, N., Hvidegaard, S. M., and Skourup, H.: Arctic Sea Ice Characterization Using Spaceborne Fully Po-
larimetric L-, C-, and X-band SAR With Validation by Airborne Measurements, IEEE Trans. Geosci. Remote Sens., 56, 3715–3734,
https://doi.org/10.1109/TGRS.2018.2809504, 2018.

Tian, L., Xie, H., Ackley, S. F., Tang, J., Mestas-Nuñez, A. M., and Wang, X.: Sea-ice freeboard and thickness in the Ross Sea from airborne
(IceBridge 2013) and satellite (ICESat 2003–2008) observations, Ann. Glaciol., 61, 24–39, https://doi.org/10.1017/aog.2019.49, 2020.

Tin, T. and Jeffries, M. O.: Sea-ice thickness and roughness in the Ross Sea, Antarctica, Ann. Glaciol., 33, 187–193,
https://doi.org/10.3189/172756401781818770, 2001.

U.S. National Ice Center.: Arctic and Antarctic Sea Ice Concentration and Climatologies in Gridded Format, Version 1,
https://doi.org/10.7265/46cc-3952, 2020.

Vernet, M., Geibert, W., Hoppema, M., Brown, P. J., Haas, C., Hellmer, H., Jokat, W., Jullion, L., Mazloff, M., Bakker, D., et al.: The Weddell
Gyre, Southern Ocean: present knowledge and future challenges, Rev. Geophys., 57, 623–708, https://doi.org/10.1029/2018RG000604,
2019.

Wakabayashi, H., Matsuoka, T., Nakamura, K., and Nishio, F.: Polarimetric Characteristics of sea ice in the sea of Okhotsk observed by
airborne L-band SAR, IEEE Trans. Geosci. Remote Sens., 42, 2412–2425, https://doi.org/10.1109/TGRS.2004.836259, 2004.

Wang, X., Jiang, W., Xie, H., Ackley, S., and Li, H.: Decadal variations of sea ice thickness in the Amundsen-Bellingshausen and
Weddell seas retrieved from ICESat and IceBridge laser altimetry, 2003–2017, J. Geophys. Res.: Oceans, 125, e2020JC016 077,
https://doi.org/10.1029/2020JC016077, 2020.

Weeks, W. F. and Ackley, S. F.: The growth, structure, and properties of sea ice, in: The geophysics of sea ice, pp. 9–164, Springer,
https://doi.org/10.1007/978-1-4899-5352-0_2, 1986.

Winebrenner, D., Farmer, L., and Joughin, I.: On the response of polarimetric synthetic aperture radar signatures at 24-cm wavelength to sea
ice thickness in Arctic leads, Radio Sci., 30, 373–402, https://doi.org/10.1029/94RS02313, 1995.

Yi, D., Egido, A., Smith, W. H., Connor, L., Buchhaupt, C., and Zhang, D.: Arctic Sea-Ice Surface Elevation Distribution from NASA's
Operation IceBridge ATM Data, Remote Sensing, 14, 3011, https://doi.org/10.3390/rs14133011, 2022.

Yitayew, T. G., Dierking, W., Divine, D. V., Eltoft, T., Ferro-Famil, L., Rösel, A., and Negrel, J.: Validation of Sea-Ice Topographic Heights Derived From TanDEM-X Interferometric SAR Data With Results From Laser Profiler and Photogrammetry, IEEE Trans. Geosci. Remote Sens., 56, 6504–6520, https://doi.org/10.1109/TGRS.2018.2839590, 2018.

500 Zwally, H. J., Yi, D., Kwok, R., and Zhao, Y.: ICESat measurements of sea ice freeboard and estimates of sea ice thickness in the Weddell Sea, J. Geophys. Res.: Oceans, 113, https://doi.org/10.1029/2007JC004284, 2008.